

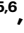
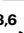

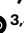



# Time-domain observation of ballistic orbital-angular-momentum currents with giant relaxation length in tungsten

Received: 13 December 2022

Accepted: 29 June 2023

Published online: 7 August 2023

 Check for updatesTom S. Seifert <sup>1,2</sup>✉, Dongwook Go <sup>3,4</sup>, Hiroki Hayashi <sup>5,6</sup>, Reza Rouzegar<sup>1,2</sup>, Frank Freimuth <sup>3,6</sup>, Kazuya Ando <sup>5,6,7</sup>, Yuriy Mokrousov <sup>3,4</sup> & Tobias Kampfrath <sup>1,2</sup>

The emerging field of orbitronics exploits the electron orbital momentum  $L$ . Compared to spin-polarized electrons,  $L$  may allow the transfer of magnetic information with considerably higher density over longer distances in more materials. However, direct experimental observation of  $L$  currents, their extended propagation lengths and their conversion into charge currents has remained challenging. Here, we optically trigger ultrafast angular-momentum transport in Ni|W|SiO<sub>2</sub> thin-film stacks. The resulting terahertz charge-current bursts exhibit a marked delay and width that grow linearly with the W thickness. We consistently ascribe these observations to a ballistic  $L$  current from Ni through W with a giant decay length (~80 nm) and low velocity (~0.1 nm fs<sup>-1</sup>). At the W/SiO<sub>2</sub> interface, the  $L$  flow is efficiently converted into a charge current by the inverse orbital Rashba–Edelstein effect, consistent with *ab initio* calculations. Our findings establish orbitronic materials with long-distance ballistic  $L$  transport as possible candidates for future ultrafast devices and an approach to discriminate Hall-like and Rashba–Edelstein-like conversion processes.

Electrons carry two distinct angular momenta: the spin angular momentum  $S$  and orbital angular momentum  $L$ . While  $S$  is successfully exploited in spintronics<sup>1</sup> to transport information by  $S$  currents and to convert them into detectable charge ( $C$ ) currents by spin-to-charge-current conversion (SCC)<sup>2</sup>,  $L$  has only recently gained attention in orbitronics research. To make this fascinating concept compatible and competitive with conventional electronics<sup>3,4</sup>, the speed of orbitronic functionalities needs to reach terahertz (THz) rates<sup>5</sup>.

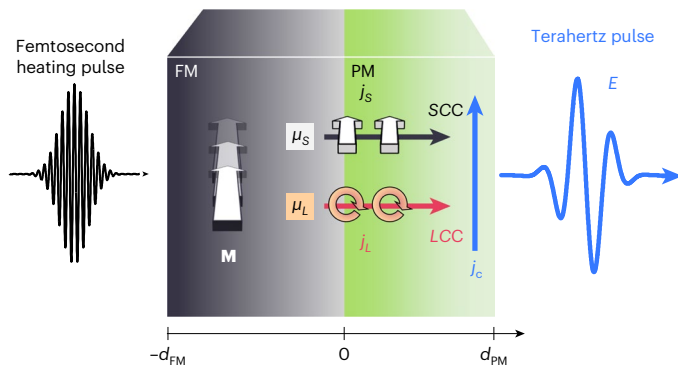
A first key advantage of  $L$  over  $S$  is that  $L$  can assume arbitrarily high values per electron and, thus, enable efficient magnetic-order manipulation<sup>1,6,7</sup> by  $L$ -induced torques<sup>8–12</sup>. Second,  $L$ -to-charge-current conversion ( $LCC$ ) works in materials without spin-orbit interaction, including abundant light metals<sup>13</sup>. Finally,  $L$  currents

are predicted to propagate over increased lengths of nearly 100 nm (ref. 14).

Recent studies provided strong indications of charge-to- $L$  current conversion by the orbital Hall effect (OHE) in a thin layer of a paramagnetic material (PM). The resulting  $L$  current was typically interrogated through the torque it exerted on the magnetization of an adjacent thin-film ferromagnetic material (FM)<sup>1,8–12,14–24</sup>. The FM was chosen to be susceptible to either an  $S$  accumulation, for example, permalloy Ni<sub>81</sub>Fe<sub>19</sub> (Py), or an  $L$  accumulation, for example, Ni.

Unfortunately, it remains experimentally challenging to measure  $L$  currents by  $LCC$ . First, it is difficult to distinguish  $LCC$  by the inverse OHE (IOHE) from  $LCC$  by an inverse orbital Rashba–Edelstein effect (IOREE) because both phenomena obey identical macroscopic

<sup>1</sup>Department of Physics, Freie Universität Berlin, Berlin, Germany. <sup>2</sup>Department of Physical Chemistry, Fritz-Haber-Institut der Max-Planck-Gesellschaft, Berlin, Germany. <sup>3</sup>Peter-Grünberg-Institut, Forschungszentrum Jülich, Jülich, Germany. <sup>4</sup>Institute of Physics, Johannes-Gutenberg-Universität Mainz, Mainz, Germany. <sup>5</sup>Department of Applied Physics and Physico-Informatics, Keio University, Yokohama, Japan. <sup>6</sup>Keio Institute of Pure and Applied Sciences, Keio University, Yokohama, Japan. <sup>7</sup>Center for Spintronics Research Network, Keio University, Yokohama, Japan. ✉e-mail: [tom.seifert@fu-berlin.de](mailto:tom.seifert@fu-berlin.de)



**Fig. 1 | Launching and detecting terahertz *S* and *L* currents.** Upon ultrafast laser excitation of the FM, an excess of FM magnetization **M** arises, leading to *S* accumulation  $\mu_S$ , *L* accumulation  $\mu_L$  and the injection of spin and orbital currents  $j_S$  and  $j_L$ , respectively, into the PM. Various bulk and interfacial *LCC* and *SCC* processes generate an ultrafast in-plane charge current  $j_c$  that emits a terahertz electromagnetic pulse with electric-field amplitude  $E(t)$  versus time  $t$  directly behind the sample.

symmetries. Second and for the same reason, IOHE and IOREE are difficult to separate from their *S* counterparts, that is, the inverse spin Hall effect (ISHE) and inverse spin Rashba–Edelstein effect (ISREE)<sup>25</sup>. Previous work, however, indicates different spatial propagation and relaxation dynamics of *S* and *L* currents<sup>8,9,14</sup>. Therefore, an experimental approach such as terahertz emission spectroscopy<sup>26,27</sup>, which monitors currents with femtosecond resolution, is perfectly suited to access the possibly different ultrafast *L*-versus-*S* propagation and conversion dynamics.

Here, we study ultrafast signatures of *S* and *L* transport from an FM into a PM that is launched by exciting FM|PM stacks with a femtosecond laser pulse (Fig. 1). The *LCC* and *SCC* in the PM are measured by monitoring the emitted terahertz pulse. Upon changing the FM from Ni to Py and interfacing it with the PMs Pt, Ti and W, we find the same characteristic sign changes in the emitted terahertz field as in previous magneto-transport studies<sup>9</sup>. Consequently, we interpret our observations as hallmarks of ultrafast *LCC* and *SCC*.

Remarkably, the terahertz field from Ni|W is temporally strongly delayed and broadened relative to that from Ni|Pt. The bandwidth and amplitude of the underlying burst of charge current decreases with W thickness, whereas its delay and width increase linearly. We assign this observation to long-distance ballistic *L* transport in W, which has a relaxation length that is more than one order of magnitude larger than that of *S* transport. Specifically, our data and calculations suggest a dominant contribution to *LCC* through the IOREE at the W/SiO<sub>2</sub> interface. This effect is absent in Ni|Ti and attributed to a dominant bulk *LCC* by the IOHE. Our results may help establish an ultrafast experimental and theoretical methodology to extract the propagation dynamics of *L* currents.

## Conceptual background

Our approach follows the idea that *L* and *S* currents have the same symmetry properties yet potentially different dynamics on ultrashort time and length scales<sup>1,8,9,14</sup>. As depicted in Fig. 1, a femtosecond optical pump pulse excites an FM|PM stack and triggers ultrafast *S* and *L* currents with density  $j_S$  and  $j_L$ , respectively, along the *z* axis from FM to PM. *SCC* and *LCC* result in ultrafast in-plane charge currents acting as sources of a terahertz electromagnetic pulse<sup>28</sup>. The resulting terahertz electric-field amplitude  $E(t)$  directly behind the sample is proportional to the sheet charge current  $I_c(t)$ , that is,

$$E(t) \propto I_c(t) = \int_{-d_{\text{FM}}}^{d_{\text{PM}}} dz [\theta_{LC}(z)j_L(z, t) + \theta_{SC}(z)j_S(z, t)]. \quad (1)$$

Here,  $d_{\text{FM}}$  and  $d_{\text{PM}}$  denote the FM and PM thickness, respectively, and  $\theta_{LC}(z)$  and  $\theta_{SC}(z)$  describe the local efficiency of the instantaneous *LCC* and *SCC*, respectively. They include microscopic mechanisms like the ISHE or IOHE<sup>27,29</sup>, occurring in the bulk, or the ISREE and IOREE, which require regions of broken inversion symmetry such as interfaces<sup>30,31</sup>. Equation (1) neglects contributions due to magnetic-dipole radiation and contributions of photocurrents even in magnetization, because both can be discriminated experimentally<sup>32,33</sup>.

To understand the emergence of  $j_S$  and  $j_L$ , we first note that sudden laser heating of the FM induces an *S* accumulation  $\mu_S$ . Here,  $\mu_S$  is proportional to the excess *S* magnetization, that is, the difference between the instantaneous *S* magnetization and the equilibrium *S* magnetization that would be attained at the instantaneous elevated electron temperature<sup>33–36</sup>. Consequently, the FM releases *S* at a rate proportional to  $\mu_S$ , by transferring *S* to both the crystal lattice through, for example, spin flips, and to the PM by, for example, a spin-current density  $j_S \propto \mu_S$ . Analogous to *S*, we expect that laser heating also induces an *L* accumulation  $\mu_L$  and, in turn, *L* transport with  $j_L \propto \mu_L$ .

Recent studies on single-element FMs like Ni showed that the *S*-type and *L*-type magnetizations exhibit very similar ultrafast dynamics following laser excitation<sup>37–39</sup>. Therefore, we expect  $\mu_L(t) \propto \mu_S(t)$ , where the ratio  $\mu_L/\mu_S$  is FM-dependent<sup>12</sup>. Despite these identical driving dynamics, the resulting  $j_L(z, t)$  and  $j_S(z, t)$  (Fig. 1) can have very different evolutions because *S* and *L* may propagate differently through the FM/PM interface and the PM bulk.

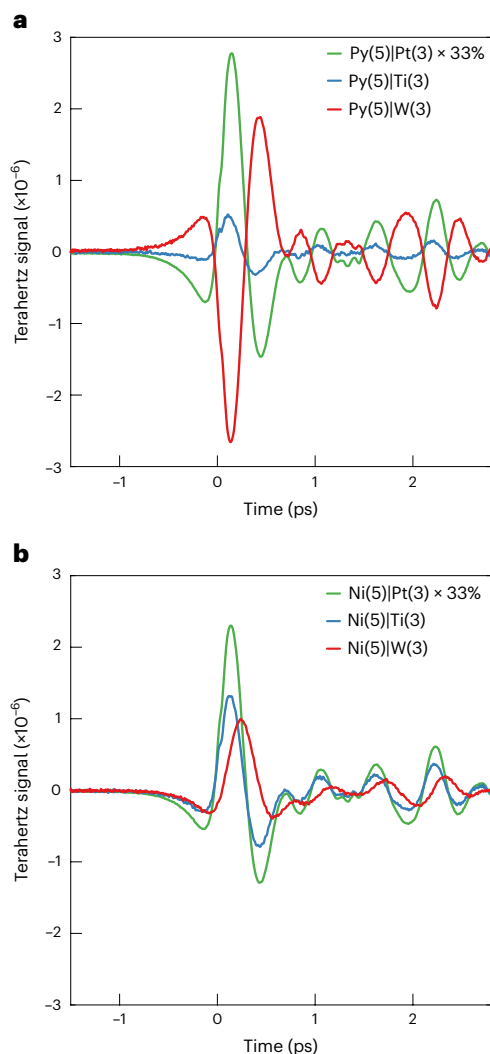
## Experiment details

We study FM|PM thin-film stacks, where the two FMs Py and Ni are chosen for their high efficiency in generating *S* and *L* currents, respectively<sup>9</sup>. The chosen PMs have a strong ISHE (Pt, W) and IOHE (W, Ti) response. The reported ISHE signs are opposite for Pt versus W, with a vanishing ISHE in Ti. By contrast, the expected IOHE signs are the same for all three PMs<sup>40</sup>. The studied FM|PM thin-film stacks are deposited onto glass (thickness, 500  $\mu\text{m}$ ) or thermally oxidized Si substrates (thickness, 625  $\mu\text{m}$ ; Supplementary Fig. 1 and Methods). They are characterized by optical and terahertz transmission spectroscopy<sup>41</sup>, yielding the pump absorbance, d.c. conductivity and Drude relaxation rate (Supplementary Fig. 2).

In our experiment (Fig. 1), ultrashort laser pulses (10 fs nominal duration, 800 nm centre wavelength, 80 MHz repetition rate, 1.9 nJ pulse energy, 0.2 mJ cm<sup>-2</sup> incident fluence) excite the sample. We record the emitted terahertz radiation by electro-optic sampling in a ZnTe(110) (thickness 1 mm or 10  $\mu\text{m}$ ) or GaP(110) (250  $\mu\text{m}$ ) crystal<sup>42</sup>. The resulting terahertz emission signal  $S_{\text{THz}}(\mathbf{M}, t)$  versus time  $t$  and sample magnetization **M** equals the terahertz electric-field waveform  $E$  (Fig. 1) convoluted with a set-up response function<sup>43</sup>. The presented data are smoothed by convolution with a Gaussian (80 fs full-width at half-maximum) for better visibility, unless noted otherwise.

All experiments are performed under ambient conditions unless stated otherwise. We apply an in-plane magnetic field of -10 mT to the sample and monitor the terahertz field component perpendicular to **M**. The component parallel to **M** is found to be minor (Supplementary Fig. 3). Measurements with linearly and circularly polarized pump pulses reveal a negligible impact of the pump polarization on the terahertz emission (Supplementary Fig. 4). We checked explicitly that  $S_{\text{THz}}(\mathbf{M}, t)$  from the Ni-based samples increases almost linearly with pump fluence (Supplementary Fig. 5).

To isolate magnetic effects, we focus on the odd-in-**M** signal  $S_{\text{THz}}(t) = [S_{\text{THz}}(+\mathbf{M}, t) - S_{\text{THz}}(-\mathbf{M}, t)]/2$ . The even-in-**M** signal components are more than two orders of magnitude smaller. Measurements on reversed samples reveal that  $S_{\text{THz}}$  predominantly arises from structural inversion asymmetry, consistent with Fig. 1. Minor contributions unrelated to structural inversion asymmetry most likely arise from magnetic-dipole radiation due to ultrafast demagnetization (Supplementary Fig. 6)<sup>33</sup>.



**Fig. 2 | Terahertz raw data.** **a, b**, Terahertz emission signals  $S_{\text{THz}}(t)$  from FM|PM stacks with FM = Py (**a**) and FM = Ni (**b**) capped with PM = Pt, W or Ti. In both panels, the Pt-based sample signals are multiplied by 33%. Film thicknesses in nanometres are given as numerals in parentheses. As a terahertz detector, a ZnTe(110) crystal (thickness 1 mm) was used.

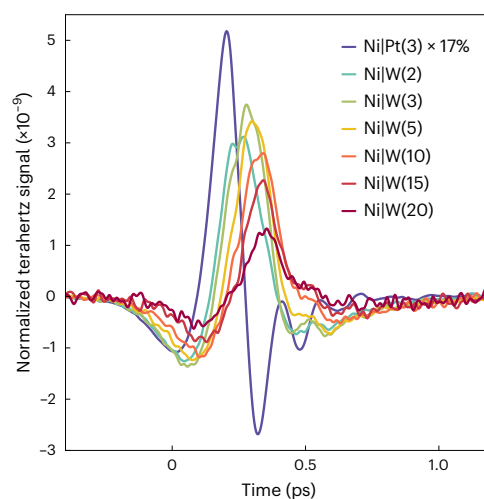
## Results

### Ferromagnetic Py versus Ni

Figure 2a shows terahertz emission signals  $S_{\text{THz}}$  from Py|PM samples, where PM is Pt, W or Ti. All three waveforms have an identical shape. Minor shape differences of  $S_{\text{THz}}^{\text{Py|Ti}}$  versus  $S_{\text{THz}}^{\text{Py|Pt}}$  are attributed to contributions unrelated to structural inversion asymmetry as described above and in Supplementary Fig. 7.

The relative signal magnitudes and the opposite polarities for PM = Pt and W are consistent with previous reports of ISHE-dominated terahertz emission<sup>28</sup>. The polarity of the Py|Ti signal is the same as that of Py|Pt and consistent with calculations and measurements, which found the same sign of the ISHE and IOHE in Pt and Ti, respectively<sup>13,27,40</sup>. Even though Ti has a sizeable LCC efficiency, our data imply  $S_{\text{THz}}^{\text{Py|Ti}} \ll S_{\text{THz}}^{\text{Py|Pt}}$ . We ascribe this observation to a small  $L$ -current amplitude injected into Ti, consistent with the small  $L$  component of the Py magnetization<sup>9</sup>.

To summarize, for Py|PM, our terahertz signals are consistent with the transport of predominantly  $S$  and  $L$  into the PM bulk and its conversion into a charge current through the ISHE and IOHE, respectively. At the FM/PM interface, a possible Rashba-type or skew-scattering-type LCC or SCC<sup>44</sup> may make an additional yet relatively small contribution.



**Fig. 3 | Impact of W thickness in Ni|W.** Terahertz emission signals for Ni|W samples with varying W thickness, normalized to the absorbed pump-pulse fraction in the Ni layer and to the sample impedance (see Methods and Supplementary Table 1). Note the rescaling of the reference signal from Ni|Pt. Film thicknesses in nanometres are given as numerals in parentheses, except for Ni, which was always 5 nm thick. A GaP(110) crystal (thickness 250  $\mu\text{m}$ ) was used as a terahertz detector.

When the FM of Py is replaced by Ni, the signal polarity remains identical for PM = Pt and Ti, and the two waveforms for the different FMs exhibit identical dynamics (Fig. 2b and Supplementary Fig. 8). By stark contrast, the signal polarity for Ni|W reverses with respect to Py|W, the waveform changes shape, and its maximum appears delayed compared to Py|W. This striking observation indicates that Py|W and Ni|W show different photocurrent mechanisms, the dominance of which depends sensitively on the FM. To understand the different dynamics in Ni|W, we next vary the W thickness.

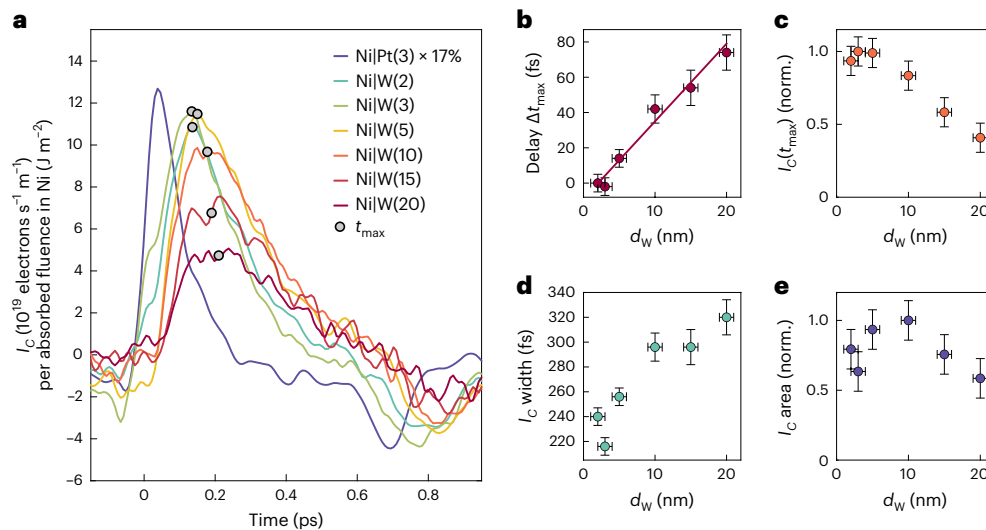
### Impact of W thickness on current dynamics in Ni|W

Figure 3 shows terahertz emission signals from Ni|W( $d_w$ ) for various W thicknesses  $d_w$  and from a Ni|Pt reference sample. Consistent with Fig. 2b, we see a clear trend with increasing  $d_w$  relative to Ni|Pt:  $S_{\text{THz}}(t)$  has the same sign, decreases with increasing  $d_w$  and reshapes considerably from being asymmetric (Ni|Pt) to being more symmetric (Ni|W) around the signal maximum. Interestingly,  $d_w = 2$  nm already induces a shift of the signal maximum by about 100 fs compared to Ni|Pt.

Notably, the changes in terahertz signal dynamics solely originate from changing the PM thickness. Therefore, the FM is considered as a PM-independent  $S$  and  $L$  injector in the following.

To obtain a sample-intrinsic measurement of the  $L$  transport and conversion dynamics, we extract the sheet charge current  $I_c(t)$  flowing in Ni|W (equation (1)) normalized to the absorbed pump-pulse fluence in Ni. This procedure eliminates any impact of sample exchange on the pump-pulse-absorption efficiency, sample impedance or set-up response function (Methods).

Figure 4a displays  $I_c(t)$  in Ni|W with a resolution of 50 fs for various W thicknesses  $d_w$ . The  $I_c(t)$  traces have striking features: (1) They exhibit the same polarity as Ni|Pt. (2) The  $I_c$  amplitude decreases approximately linearly with  $d_w$  to about 50% after 20 nm (Fig. 4c), indicating attenuation and dispersion upon propagation. (3) The  $I_c$  maximum shifts by delays  $\Delta t_{\text{max}} \propto d_w$  relative to  $d_w = 2$  nm at a rate of  $\Delta t_{\text{max}}/d_w \approx 4$  fs  $\text{nm}^{-1}$  (Fig. 4b), implying a velocity of 0.25 nm  $\text{fs}^{-1}$ . (4) The  $I_c$  width increases linearly at a rate of  $\approx 8$  fs  $\text{nm}^{-1}$  (Fig. 4d). (5) The time-integrated current  $\int dt I_c(t)$  only weakly decreases with  $d_w$ , thereby indicating an extremely large relaxation length of  $>20$  nm (Fig. 4e)<sup>8,9,14</sup>.



**Fig. 4 | Ultrafast charge currents in Ni|W.** **a**, Charge sheet currents  $I_c(t)$  in Ni|W for various W thicknesses  $d_w$  as extracted from the data of Fig. 3. The feature at 0.8 ps is a remainder of a terahertz field reflection echo in the 10  $\mu$ m ZnTe electro-optic detection crystal (Methods). Film thicknesses in nanometres are given as numerals in parentheses, except for Ni, which was always 5 nm thick. Note the rescaling of the Pt-based sample signal. The apparent signal maxima

$I_c(t_{max})$  values are highlighted by circular markers. **b**, Extracted time delay  $\Delta t_{max}$  relative to Ni(5 nm)|W(2 nm) with a straight line as a guide to the eye. **c**, Relative (normalized, norm.) amplitude of  $I_c(t_{max})$ . **d**, Full-width of  $I_c(t)$  at half-maximum. **e**, Time-integrated  $I_c(t)$  over 0.0–0.7 ps versus  $d_w$  from the data in **a**. Details of the error estimates are given in Methods.

Feature (1) implies that  $I_c(t)$  cannot arise from  $S$  transport. The reason is that the ISHE dominates the SCC in Pt and W, yet with opposite sign<sup>28,45</sup>. This conclusion is strongly supported by feature (2) because an  $S$  current in W would relax over distances of  $\ll 20$  nm (refs. 41,46). Our data, therefore, strongly indicate that  $L$  transport plus LCC dominates the terahertz charge current in Ni|W.

Features (3) and (4) indicate a signal arising from ballistic-like transport of a pulse that is detected in an arrival layer. In this picture, the increasing width of  $I_c(t)$  with  $d_w$  arises from a velocity dispersion along the  $z$  direction of the particles inside the pulse (Fig. 5a). Feature (5) implies a minor LCC in the W bulk because the integrated charge current  $\int dt I_c(t)$  would increase monotonically with  $d_w$  otherwise.

### Model of $L$ current and IOREE in Ni|W

The preceding discussion suggests the following transport scenario in Ni|W. Excitation of the Ni layer induces a transient  $S$  and  $L$  accumulation (Fig. 1) with very similar dynamics as described previously<sup>37–39</sup>. The resulting  $L$  accumulation  $\mu_L(t) \propto \mu_S(t)$  is monitored well by the ISHE charge current in Ni|Pt (Fig. 4a). It injects  $L$ -polarized electron wave packets into W, that is, coherent superpositions of Bloch states with non-zero net  $L$  (ref. 1; Fig. 5a). Finally, regions close to the W/SiO<sub>2</sub> interface dominate the LCC. This interpretation is strongly supported by our ab initio calculations (Methods and Supplementary Figs. 9–11). The calculated  $L$  velocity ( $\sim 0.1$  nm fs<sup>-1</sup>; Supplementary Fig. 10) agrees well with our measurements (Fig. 4b). The calculated LCC (Supplementary Fig. 11) reveals a giant interfacial contribution (IOREE) in a thin W film with the same sign as the ISHE in Pt (Fig. 4a). An efficient interfacial LCC was already invoked previously<sup>7,24,47–51</sup>.

The suggested scenario explains all experimental charge-current features (1)–(5) (Fig. 4). As the  $j_L$  pulse propagates predominantly ballistically through W, its arrival in the W/SiO<sub>2</sub> LCC region is delayed by a time  $\Delta t_{max} \propto d_w$ . Likewise,  $j_L$  disperses due to different electron-velocity  $z$ -axis projections (Fig. 5a) and relaxes over a length of  $> 20$  nm.

To model the charge-current dynamics in Ni|W (Fig. 4), we assume  $j_L$  is solely driven by  $\mu_L$  and, thus, given by the linear-response relationship (convolution)

$$j_L(z, t) = (r_z * \mu_L)(t) = \int_{-\infty}^{+\infty} d\tau r_z(t - \tau) \mu_L(\tau). \quad (2)$$

Here,  $r_z$  is the  $L$  current density at position  $z$  following a fictitious  $\delta(t)$ -like  $L$  accumulation in Ni, and  $\mu_L(t) \propto \mu_S(t)$  is given by the measured Ni|Pt charge current (Fig. 4a). Assuming an instantaneous IOREE response at  $z = d_w$ ,  $I_c(t)$  is proportional to  $j_L(d_w, t)$ .

In the Methods, we analytically calculate the response function  $r_z$  for the cases of ballistic transport (equations (9) and (10) and Fig. 5b) and diffusive transport (equation (12)). For ballistic transport, the modelled  $I_c(t)$  curves (Fig. 5c) reproduce the measured Ni|W charge currents (Fig. 4a) semiquantitatively for a relaxation length of 80 nm and a dominant  $L$  wave-packet velocity of  $v_L = 0.14$  nm fs<sup>-1</sup>. These values agree well with the estimates given previously (Fig. 4b–e) and with the calculated orbital velocity (Supplementary Fig. 10). We did not attempt to obtain even better agreement of the modelled and measured  $I_c(t)$  by considering different distributions of the  $L$  velocity directions (Fig. 5a and equation (9)).

By contrast, for diffusive transport, our model reproduces the experimental data less favourably (Supplementary Fig. 12). Therefore, the observed  $L$  currents (Fig. 4) have a significant ballistic component.

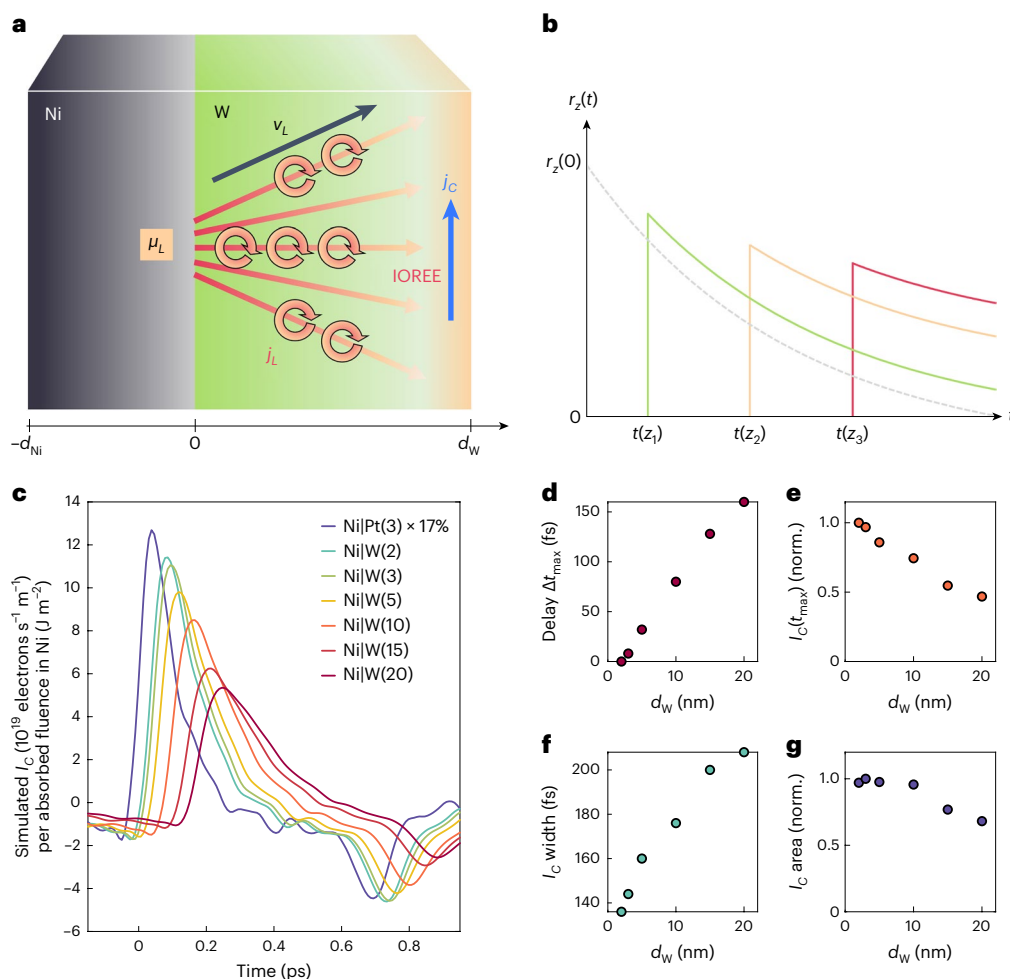
To summarize, the terahertz charge currents in Ni|W (Fig. 4) arise from  $L$  currents injected into W. The charge-current generation (equation (1)) is dominated by LCC at the W/SiO<sub>2</sub> interface. The extremely long-range  $j_L$  in W is a unique feature of orbitronic materials, first indications of which were found previously in Ti (refs. 8,9).

### Discussion

Our interpretation neglects other possible contributions to  $I_c(t)$ . First, the pump polarization independence rules out the inverse Faraday effect as a source of  $S$  (ref. 52) and  $L$  currents (Supplementary Fig. 4).

Second, for  $j_S$ , a dominant Seebeck-type contribution from an electronic temperature difference  $\Delta T_{FM/PM}$  across the Ni/PM interface is negligible<sup>33</sup>. For  $j_L$ , we estimate  $\Delta T_{Ni/PM}$  after pump-pulse absorption (Methods) and find  $\Delta T_{Ni/Pt} = +400$  K and  $\Delta T_{Ni/PM} = -100$  K for PM = Ti or





**Fig. 5 | Model of  $L$  transport and IOREE in W.** **a**, Schematic of the suggested scenario for  $L$  transport and LCC by the IOREE in Ni|W. The impulsive  $L$  accumulation  $\mu_L$  launches  $L$  wave packets of various velocities  $v_L$  and, thus, an orbital current  $j_L$  into the W layer. Upon reaching the W back surface,  $j_L$  is converted into a transverse charge current  $j_c$  by the IOREE. In the experiment, the orbital currents of all point-like sources add up at the Ni/W interface. **b**, Qualitative ballistic current densities  $r_z(t)$  in response to a fictitious  $\delta(t)$ -like  $\mu_L$  at different

positions  $z_1 < z_2 < z_3$  in W. **c**, Simulated IOREE charge currents  $I_c(t)$  obtained by equation (2) in the case of ballistic transport. Parameters are the  $L$  wave-packet velocity ( $|v_L| = 0.14$  fs  $\text{nm}^{-1}$ ); **a**, the  $j_L$  decay length (80 nm) and a global scaling factor. **d**, Extracted time delay  $\Delta t_{\text{max}}$  relative to Ni(5 nm)|W(2 nm). **e**, Relative amplitude of  $I_c(t_{\text{max}})$ . **f**, Full-width of  $I_c(t)$  at half-maximum. **g**, Time-integrated  $I_c(t)$  over 0.0–0.7 ps versus  $d_w$  from the data in **c**.

W. The observed terahertz emission signals, by contrast, have the same sign for all three samples (Fig. 2b). Therefore, interfacial electronic temperature differences have a minor impact on  $L$  and  $S$  transport. Simulations further show that pump-intensity gradients in the FM and PM bulk are relatively small (Supplementary Fig. 13).

Third, angular-momentum transport in W by magnons is neglected because W is magnetically disordered. Acoustic phonons are excluded because the sound velocity in W is  $< 0.01$  nm  $\text{fs}^{-1}$  (ref. 53) and, thus, considerably below the observed transport velocity. An outstandingly long-range  $S$  propagation is ruled out because the Drude scattering times of all samples are  $< 50$  fs (Supplementary Fig. 2) and, thus, substantially shorter than the  $I_c(t)$  peak delays (Fig. 4b).

Fourth, even though the IOREE dominates the charge-current generation in Ni|W, the positive shoulder-like feature at around time zero for  $d_w \leq 3$  nm in Fig. 4a may indicate a small contribution of bulk LCC, that is, the IOHE, consistent with the IOHE sign in W. An  $L$ -to- $S$  conversion plus ISHE in the PM<sup>23</sup> might contribute but is considered negligible here given the good agreement of the measurements (Fig. 4) and model (Fig. 5). The dominance of  $j_L$  in Ni|W highlights the role of Ni as an  $L$ -current source and indicates that the Ni/W interface may transmit  $j_L$  more efficiently than  $j_S$ .

Interestingly, a detailed comparison of Fig. 2a,b reveals pronounced amplitude changes for PM = W or Pt when changing the FM from Py to Ni. These differences are related to the intricate interplay of all parameters in equation (1), in addition to relative changes of  $\mu_S$  and  $\mu_L$  and of interface transmission coefficients for  $j_S$  and  $j_L$ .

We emphasize that samples deposited on Si rather than glass substrates show very similar terahertz emission characteristics (Supplementary Fig. 1), demonstrating the robustness of the observed effects. When adding a Cu layer on top of the Ni|W sample, we find similar terahertz emission signals (Supplementary Fig. 14). Interestingly, a Cu interlayer in Ni|Cu|W only slightly modifies the terahertz signal, suggesting that Cu does not block  $L$  transport strongly.

Regarding earlier reports of different terahertz emission dynamics in Fe|Au and Fe|Ru samples<sup>29</sup>, we note that a possible IOREE in Ru seems possible in hindsight. This interpretation might explain the seemingly strong dependence of the Fe|Ru terahertz emission dynamics on growth details<sup>29,54,55</sup>.

## Conclusions

We observe terahertz emission signals from optically excited Ni|W stacks that are consistently assigned to the ultrafast injection of  $L$

currents into  $W$  and long-distance ballistic transport through  $W$ . Remarkably, we find strong indications for a dominant IOREE in both experiment and theory. This result can be considered as time-domain signature of the long-range nature of orbital currents and the IOREE in  $W$ .

Our study highlights the power of broadband terahertz emission spectroscopy in disentangling  $S$  and  $L$  transport as well as Hall-like and Rashba–Edelstein-like conversion processes based on their dynamics. We find that  $Py$  versus  $Ni$  are, respectively, attractive  $S$  and  $L$  sources, whereas  $Pt$  versus  $W$  are, respectively, good  $S$ -to-charge and  $L$ -to-charge converters with distinctly different efficiency and dynamics for  $S$  versus  $L$ . We believe that our results are a significant step toward the identification of ideal sources and detectors of either  $S$  or  $L$  currents, which will strongly benefit from accurate theoretical predictions.

## Online content

Any methods, additional references, Nature Portfolio reporting summaries, source data, extended data, supplementary information, acknowledgements, peer review information; details of author contributions and competing interests; and statements of data and code availability are available at <https://doi.org/10.1038/s41565-023-01470-8>.

## References

- Go, D., Jo, D., Lee, H. W., Klaui, M. & Mokrousov, Y. Orbitronics: orbital currents in solids. *EPL* **135**, 37001 (2021).
- Miron, I. M. et al. Perpendicular switching of a single ferromagnetic layer induced by in-plane current injection. *Nature* **476**, 189–193 (2011).
- Ji, B. et al. Several key technologies for 6G: challenges and opportunities. *IEEE Commun. Stand. Mag.* **5**, 44–51 (2021).
- Schwierz, F. J. & Liou, J. RF transistors: recent developments and roadmap toward terahertz applications. *Solid State Electron.* **51**, 1079–1091 (2007).
- Vedmedenko, E. Y. et al. The 2020 magnetism roadmap. *J. Phys. D: Appl. Phys.* **53**, 453001 (2020).
- Salemi, L., Berritta, M., Nandy, A. K. & Oppeneer, P. M. Orbitally dominated Rashba-Edelstein effect in noncentrosymmetric antiferromagnets. *Nat. Commun.* **10**, 5381 (2019).
- Johansson, A., Göbel, B., Henk, J., Bibes, M. & Mertig, I. Spin and orbital Edelstein effects in a two-dimensional electron gas: theory and application to  $SrTiO_3$  interfaces. *Phys. Rev. Res.* **3**, 013275 (2021).
- Bose, A. et al. Detection of long-range orbital-Hall torques. *Phys. Rev. B* **107**, 134423 (2023).
- Hayashi, H. et al. Observation of long-range orbital transport and giant orbital torque. *Commun. Phys.* **6**, 32 (2023).
- Zheng, Z. C. et al. Magnetization switching driven by current-induced torque from weakly spin-orbit coupled  $Zr$ . *Phys. Rev. Res.* **2**, 013127 (2020).
- Kim, J. et al. Nontrivial torque generation by orbital angular momentum injection in ferromagnetic-metal/ $Cu/Al_2O_3$  trilayers. *Phys. Rev. B* **103**, L020407 (2021).
- Lee, D. et al. Orbital torque in magnetic bilayers. *Nat. Commun.* **12**, 6710 (2021).
- Choi, Y. G. et al. Observation of the orbital Hall effect in a light metal  $Ti$ . *Nature* **619**, 52–56 (2023).
- Go, D. et al. Long-range orbital torque by momentum-space hotspots. *Phys. Rev. Lett.* **130**, 246701 (2023).
- An, H., Kageyama, Y., Kanno, Y., Enishi, N. & Ando, K. Spin-torque generator engineered by natural oxidation of  $Cu$ . *Nat. Commun.* **7**, 13069 (2016).
- Seifert, T. S. et al. Femtosecond formation dynamics of the spin Seebeck effect revealed by terahertz spectroscopy. *Nat. Commun.* **9**, 2899 (2018).
- Go, D. et al. Theory of current-induced angular momentum transfer dynamics in spin-orbit coupled systems. *Phys. Rev. Res.* **2**, 033401 (2020).
- Go, D. & Lee, H. W. Orbital torque: torque generation by orbital current injection. *Phys. Rev. Res.* **2**, 013177 (2020).
- Tazaki, Y. et al. Current-induced torque originating from orbital current. Preprint at *arXiv* <https://doi.org/10.48550/arXiv.2004.09165> (2020).
- Lee, S. et al. Efficient conversion of orbital Hall current to spin current for spin-orbit torque switching. *Commun. Phys.* **4**, 234 (2021).
- Liao, L. et al. Efficient orbital torque in polycrystalline ferromagnetic-metal /  $Ru$  /  $Al_2O_3$  stacks: theory and experiment. *Phys. Rev. B* **105**, 104434 (2022).
- Xiao, Z. Y. et al. Enhancement of torque efficiency and spin Hall angle driven collaboratively by orbital torque and spin-orbit torque. *Appl. Phys. Lett.* **121**, 072404 (2022).
- Sala, G. & Gambardella, P. Giant orbital Hall effect and orbital-to-spin conversion in  $3d$ ,  $5d$ , and  $4f$  metallic heterostructures. *Phys. Rev. Res.* **4**, 033037 (2022).
- Ding, S. et al. Harnessing orbital-to-spin conversion of interfacial orbital currents for efficient spin-orbit torques. *Phys. Rev. Lett.* **125**, 177201 (2020).
- Manchon, A. et al. Current-induced spin-orbit torques in ferromagnetic and antiferromagnetic systems. *Rev. Mod. Phys.* **91**, 035004 (2019).
- Seifert, T. S., Cheng, L., Wei, Z., Kampfrath, T. & Qi, J. Spintronic sources of ultrashort terahertz electromagnetic pulses. *Appl. Phys. Lett.* **120**, 180401 (2022).
- Xu, Y. et al. Inverse orbital Hall effect discovered from light-induced terahertz emission. Preprint at *arXiv* <https://doi.org/10.48550/arXiv.2208.01866> (2022).
- Seifert, T. et al. Efficient metallic spintronic emitters of ultra-broadband terahertz radiation. *Nat. Photon.* **10**, 483–488 (2016).
- Kampfrath, T. et al. Terahertz spin current pulses controlled by magnetic heterostructures. *Nat. Nanotechnol.* **8**, 256–260 (2013).
- Jungfleisch, M. B. et al. Control of terahertz emission by ultrafast spin-charge current conversion at Rashba interfaces. *Phys. Rev. Lett.* **120**, 207207 (2018).
- Zhou, C. et al. Broadband terahertz generation via the interface inverse Rashba-Edelstein effect. *Phys. Rev. Lett.* **121**, 086801 (2018).
- Zhang, W. et al. Ultrafast terahertz magnetometry. *Nat. Commun.* **11**, 4247 (2020).
- Rouzegar, R. et al. Laser-induced terahertz spin transport in magnetic nanostructures arises from the same force as ultrafast demagnetization. *Phys. Rev. B* **106**, 144427 (2022).
- Lichtenberg, T., Beens, M., Jansen, M. H., Koopmans, B. & Duine, R. A. Probing optically induced spin currents using terahertz spin waves in noncollinear magnetic bilayers. *Phys. Rev. B* **105**, 144416 (2022).
- Mueller, B. Y. & Rethfeld, B. Thermodynamic  $\mu T$  model of ultrafast magnetization dynamics. *Phys. Rev. B* **90**, 144420 (2014).
- Choi, G. M., Min, B. C., Lee, K. J. & Cahill, D. G. Spin current generated by thermally driven ultrafast demagnetization. *Nat. Commun.* **5**, 4334 (2014).
- Boeglin, C. et al. Distinguishing the ultrafast dynamics of spin and orbital moments in solids. *Nature* **465**, 458–461 (2010).
- Stamm, C., Pontius, N., Kachel, T., Wietstruck, M. & Durr, H. A. Femtosecond X-ray absorption spectroscopy of spin and orbital angular momentum in photoexcited  $Ni$  films during ultrafast demagnetization. *Phys. Rev. B* **81**, 104425 (2010).
- Hennecke, M. et al. Angular momentum flow during ultrafast demagnetization of a ferrimagnet. *Phys. Rev. Lett.* **122**, 157202 (2019).
- Salemi, L. & Oppeneer, P. M. First-principles theory of intrinsic spin and orbital Hall and Nernst effects in metallic monoatomic crystals. *Phys. Rev. Mater.* **6**, 095001 (2022).

41. Seifert, T. S. et al. Terahertz spectroscopy for all-optical spintronic characterization of the spin-Hall-effect metals Pt, W and  $\text{Cu}_{80}\text{Ir}_{20}$ . *J. Phys. D Appl. Phys.* **51**, 364003 (2018).
42. Huber, R., Brodschelm, A., Tauser, F. & Leitenstorfer, A. Generation and field-resolved detection of femtosecond electromagnetic pulses tunable up to 41 THz. *Appl. Phys. Lett.* **76**, 3191–3193 (2000).
43. Braun, L. et al. Ultrafast photocurrents at the surface of the three-dimensional topological insulator  $\text{Bi}_2\text{Se}_3$ . *Nat. Commun.* **7**, 13259 (2016).
44. Gueckstock, O. et al. Terahertz spin-to-charge conversion by interfacial skew scattering in metallic bilayers. *Adv. Mater.* **33**, e2006281 (2021).
45. Tanaka, T. et al. Intrinsic spin Hall effect and orbital Hall effect in  $4d$  and  $5d$  transition metals. *Phys. Rev. B* **77**, 165117 (2008).
46. Demasius, K.-U. et al. Enhanced spin-orbit torques by oxygen incorporation in tungsten films. *Nat. Commun.* **7**, 10644 (2016).
47. Ding, S. et al. Observation of the orbital Rashba-Edelstein magnetoresistance. *Phys. Rev. Lett.* **128**, 067201 (2022).
48. Santos, E. et al. Inverse orbital torque via spin-orbital intertwined states. *Phys. Rev. Appl.* **19**, 014069 (2023).
49. Okano, G., Matsuo, M., Ohnuma, Y., Maekawa, S. & Nozaki, Y. Nonreciprocal spin current generation in surface-oxidized copper films. *Phys. Rev. Lett.* **122**, 217701 (2019).
50. Yoda, T., Yokoyama, T. & Murakami, S. Orbital edelstein effect as a condensed-matter analog of solenoids. *Nano Lett.* **18**, 916–920 (2018).
51. Go, D. et al. Toward surface orbitronics: giant orbital magnetism from the orbital Rashba effect at the surface of  $sp$ -metals. *Sci. Rep.* **7**, 46742 (2017).
52. Huisman, T. J. et al. Femtosecond control of electric currents in metallic ferromagnetic heterostructures. *Nat. Nanotechnol.* **11**, 455–458 (2016).
53. Hixson, R. & Winkler, M. A. Thermophysical properties of solid and liquid tungsten. *Int. J. Thermophys.* **11**, 709–718 (1990).
54. Wu, Y. et al. High-performance THz emitters based on ferromagnetic/nonmagnetic heterostructures. *Adv. Mater.* **29**, 1603031 (2017).
55. Zhang, S. et al. Bursts of efficient terahertz radiation with saturation effect from metal-based ferromagnetic heterostructures. *J. Phys. D Appl. Phys.* **51**, 034001 (2017).

**Publisher's note** Springer Nature remains neutral with regard to jurisdictional claims in published maps and institutional affiliations.

**Open Access** This article is licensed under a Creative Commons Attribution 4.0 International License, which permits use, sharing, adaptation, distribution and reproduction in any medium or format, as long as you give appropriate credit to the original author(s) and the source, provide a link to the Creative Commons license, and indicate if changes were made. The images or other third party material in this article are included in the article's Creative Commons license, unless indicated otherwise in a credit line to the material. If material is not included in the article's Creative Commons license and your intended use is not permitted by statutory regulation or exceeds the permitted use, you will need to obtain permission directly from the copyright holder. To view a copy of this license, visit <http://creativecommons.org/licenses/by/4.0/>.

© The Author(s) 2023

## Methods

### Current extraction

To extract the in-plane sheet current  $I_c$  flowing inside the sample from the measured terahertz signal  $S_{\text{THz}}$ , we first measure our set-up response function  $H_{SE}$  by having a reference electro-optic emitter (50  $\mu\text{m}$  GaP on a 500  $\mu\text{m}$  glass substrate) at the same position as the sample, which yields a reference terahertz signal  $S_{\text{THz}}^{\text{ref}}$ . By calculating the emitted terahertz electric field  $E^{\text{ref}}$  from that reference emitter,  $H_{SE}$  is determined by solving the convolution  $S_{\text{THz}}^{\text{ref}}(t) = (H_{SE} * E^{\text{ref}})(t)$  (equation (2)) for  $H_{SE}$  (ref. 43). Further measured inputs for this calculation are the excitation spot size with a full-width at half-maximum of 22  $\mu\text{m}$ , the excitation pulse energy of 1.9 nJ and a Fourier-transform-limited pump pulse with a spectrum centred at 800 nm and a full-width at half-maximum of 110 nm. We perform the deconvolution directly in the time domain by recasting it as a matrix equation<sup>16</sup>.

Next, the electric field  $E$  directly behind the sample is obtained from the recorded terahertz signal  $S_{\text{THz}}$  with the help of the derived function  $H_{SE}$  by solving the analogous equation  $S_{\text{THz}}(t) = (H_{SE} * E)(t)$  for  $E$ . Finally, the sheet charge current (Supplementary Table 1) as shown in Fig. 3 is derived from a generalized Ohm's law<sup>28</sup>, which in the frequency domain at frequency  $\omega/2\pi$  reads

$$E(\omega) = eZ(\omega)I_c(\omega). \quad (3)$$

Here,  $-e$  is the electron charge and the sample impedance  $Z(\omega)$  is given by  $Z_0/[1 + n_{\text{sub}} + Z_0d\sigma(\omega)]$  with the free-space impedance  $Z_0$ , the substrate refractive index  $n_{\text{sub}} \approx 2$  (ref. 56) and the metal-stack thickness  $d = d_{\text{FM}} + d_{\text{PM}}$ . The measured mean sample conductivity  $\sigma$  (Supplementary Table 1) is approximately frequency-independent due to the large Drude scattering rate (Supplementary Fig. 2). To enable a comparison of terahertz currents from different samples, we normalize  $I_c$  by the absorbed fluence in the FM. The data shown in Fig. 3 were obtained in a dry-air atmosphere.

### Sample preparation

The FM|PM samples (FM = Ni and Py, PM = Pt, Ti, Cu and W) are fabricated on glass substrates (thickness 500  $\mu\text{m}$ ) or thermally oxidized Si substrates (625  $\mu\text{m}$ ) by radio-frequency magnetron sputtering under an Ar atmosphere of 6N purity. The sample structure and thickness are described in Supplementary Table 1. For the sputtering, the base pressure in the chamber is lower than  $5 \times 10^{-7}$  Pa. To avoid oxidation,  $\text{SiO}_2$  (thickness 4 nm) is sputtered on the surface of the films. All sputtering processes are performed at room temperature. The W films are predominantly in the  $\beta$ -phase for  $d_{\text{W}} < 10$  nm, with an  $\alpha$ -phase content that grows with  $d_{\text{W}}$  and dominates for  $d_{\text{W}} > 10$  nm (ref. 9).

### Estimate of electronic temperatures

We calculate the electronic temperature increase  $\Delta T_{e0}$  upon pump-pulse absorption by

$$\Delta T_{e0} = \sqrt{T_0^2 + \frac{2F_l}{\gamma d}} - T_0. \quad (4)$$

Here,  $T_0 = 300$  K is the ambient temperature,  $F_l$  is the absorbed fluence in the respective layer  $l = \text{FM}$  or  $\text{PM}$  (Supplementary Table 1),  $d$  is the layer thickness and  $\gamma T_e$  is the specific electronic heat capacity at electronic temperature  $T_e$  with  $\gamma = 300 \text{ J m}^{-3} \text{ K}^{-2}$  for W,  $320 \text{ J m}^{-3} \text{ K}^{-2}$  for Ni,  $330 \text{ J m}^{-3} \text{ K}^{-2}$  for Ti and  $90 \text{ J m}^{-3} \text{ K}^{-2}$  for Pt (ref. 57).

To obtain the absorbed fluences in each layer, we note that the pump electric field is almost constant throughout the sample (Supplementary Fig. 9). Therefore, the local pump absorption scales solely with the imaginary part  $\text{Im}\epsilon$  of the dielectric function  $\epsilon$  at a wavelength of 800 nm, which equals 22.07 for Ni, 9.31 for Pt, 19.41

for Ti and 19.71 for W (ref. 58). Consequently, the absorbed fluence is determined by

$$F_l = F_{\text{tot}} \frac{d_l \text{Im}\epsilon_l}{d_{\text{FM}} \text{Im}\epsilon_{\text{FM}} + d_{\text{PM}} \text{Im}\epsilon_{\text{PM}}} \quad (5)$$

with the total absorbed fluence  $F_{\text{tot}}$  that is obtained from the absorbed pump power (Supplementary Table 1) and the beam size on the sample (as described previously).

### Experimental error estimation

The error bars for the maximum position  $t_{\text{max}}$  of the transient charge current  $I_c(t)$  (Fig. 4b) are estimated as  $\pm 20\%$  of the read-off delay value (circular markers in Fig. 4a), but no less than 5 fs. The uncertainty in the relative amplitude of  $I_c(t_{\text{max}})$  (Fig. 4c) and the relative area of  $I_c(t)$  (Fig. 4e) is, respectively, estimated as  $\pm 20\%$  and  $\pm 10\%$ , both reflecting the typical signal-to-noise ratio of the extracted current traces (Fig. 4a). The error bars for the full-width of  $I_c(t)$  at half-maximum (Fig. 4d) are obtained from the uncertainty of the delay (Fig. 4b) with subsequent multiplication by  $\sqrt{2}$ , which accounts for the error propagation of a difference of two quantities.

### Model of $L$ transport

To model the ballistic current in the PM, we assume that a  $\delta(t)$ -like transient  $L$  accumulation in the FM generates an electronic wave packet, which has orbital angular momentum  $\Delta L_{k0}$  along the direction of the FM magnetization  $\mathbf{M}$  and mean wave vector  $\mathbf{k}$  in the PM right behind the FM/PM interface, that is, at  $z = 0^+$  (Fig. 5a).

In the case of purely ballistic transport, this wave packet propagates into the PM bulk according to  $\Delta L_{k0}(z, t) = \Delta L_{k0} \delta(z - v_{kz}t)$ , where  $v_{kz}$  is the  $z$  component of the wave-packet group velocity. Note that we restrict ourselves to  $\mathbf{k}$  values with non-negative  $v_{kz}$  values. The total pump-induced  $L$  current density flowing into the depth of the PM is for  $z > 0$  given by the sum

$$r_z(t) = \sum_{\mathbf{k}, v_{kz} \geq 0} \Delta L_{k0} v_{kz} \delta(z - v_{kz}t). \quad (6)$$

Assuming that  $\Delta L_{k0}$  arises from states not too far from the Fermi energy, the summation of equation (6) is approximately proportional to an integration over the Fermi surface parts with  $v_{kz} \geq 0$ . One obtains

$$r_z(t) = e^{-t/\tau} \int_0^\infty dv_z w(v_z) v_z \delta(z - v_z t) \quad (7)$$

where  $z > 0$ , and

$$w(v_z) = \sum_{\mathbf{k}, v_{kz} \geq 0} \Delta L_{k0} \delta(v_{kz} - v_z) \quad (8)$$

is the  $L$  weight of the  $z$ -axis group velocity  $v_z$ . In equation (7), we phenomenologically account for the relaxation of the ballistic current with time constant  $\tau$  by introducing the factor  $e^{-t/\tau}$ . Performing the integration of equation (7) yields

$$r_z(t) = \frac{e^{-t/\tau}}{t} \int_0^\infty dz w\left(\frac{z}{t}\right). \quad (9)$$

To determine a plausible shape of  $w(v)$ , we note that  $\Delta L_{k0}$  is non-zero within several 0.1 eV around the Fermi energy  $E_F$  owing to the width of the photoexcited and rapidly relaxing electron distribution<sup>33</sup>. Assuming a spherical Fermi surface and isotropic  $\Delta L_{k0}$ , we have  $\Delta L_{k0} \propto \delta(E_{\mathbf{k}} - E_F)$  and  $v_{kz} = v_F \cos\theta$ , where  $E_{\mathbf{k}}$  is the band structure,  $v_F$  is the Fermi velocity and  $\theta$  is the angle between  $\mathbf{k}$  and the  $z$  axis.



Therefore, after turning equation (8) into an integral, the integrand  $\Delta L_{\mathbf{k}0} \delta(v_F \cos\theta - v_z) d^3\mathbf{k}$  becomes proportional to  $\delta(v_F \cos\theta - v_z) d\cos\theta$  in spherical coordinates, leading to

$$w(v_z) \propto \int_0^1 d\cos\theta \delta(v_F \cos\theta - v_z) \propto \Theta(v_F - v_z), \quad (10)$$

where  $\Theta$  is the Heaviside step function. In other words, all velocities  $v_z = v_F \cos\theta$  from 0 to  $v_F$  have equal weight.

In the case of purely diffusive transport, we use the  $L$  diffusion equation for  $\mu_L$  (ref. 23). With a localized accumulation  $\mu_L(z, t) \propto \delta(z)$  at time  $t \approx 0$ , the accumulation disperses according to the well-known solution

$$\mu_L(z, t) \propto \frac{1}{\sqrt{Dt}} \exp\left(-\frac{z^2}{4Dt}\right) \quad (11)$$

for  $z > 0$  and  $t > 0$ . Here,  $D$  is the diffusion coefficient that equals  $v_L^2 \tau / 3$  in the case of a spherical  $\mathbf{k}$ -space surface carrying the  $L$  wave packets,  $v_L$  is their mean group velocity, and  $\tau$  is their velocity relaxation time. To determine the current density, we apply Fick's law<sup>23</sup>  $j_L = -D \partial \mu_L / \partial z$  to equation (11) and obtain

$$r_z(t) \propto \Theta(t) \frac{z}{t} \frac{1}{\sqrt{Dt}} \exp\left(-\frac{z^2}{4Dt}\right). \quad (12)$$

### Ab initio estimate of the $L$ velocity

The orbital velocity is estimated for the bulk W in a body-centred cubic structure. The ab initio self-consistent calculation of the electronic states is performed within density functional theory by using the FLEUR code<sup>2</sup>, which implements the full-potential linearly augmented plane-wave (FLAPW) method<sup>59</sup>. The exchange-correlation effect is included in the scheme of the generalized gradient approximation by using the Perdew–Burke–Ernzerhof functional<sup>60</sup>. The lattice parameter of the cubic unit cell is set to  $5.96a_0$ , where  $a_0$  is the Bohr radius. For the muffin-tin potential, we set  $R_{\text{MT}} = 2.5a_0$  for the radius and  $l_{\text{max}} = 12$  for the maximum of the harmonic expansion. Further, we set the plane-wave cut-offs for the interstitial region to  $4.0a_0^{-1}$ ,  $10.1a_0^{-1}$  and  $12.2a_0^{-1}$  for the basis set, the exchange-correlation functional and the charge density, respectively. For the  $\mathbf{k}$ -points, a  $16 \times 16 \times 16$  Monkhorst–Pack mesh is defined.

From the converged electronic structure, we obtain the maximally localized Wannier functions by using the WANNI90 code<sup>61</sup>. We use 18 Wannier states with  $s, p_x, p_y, p_z, d_{z^2}, d_{x^2-y^2}, d_{xy}, d_{yz}, d_{zx}$  symmetries for spin up and down as the initial guess. The maximum of the inner (frozen) energy window is set 5 eV above the Fermi energy for the disentanglement, and the outer energy window is defined by the minimum and maximum energies of the 36 valence states obtained from the FLAPW calculation. The Hamiltonian and the position, orbital-angular-momentum and spin-angular-momentum operators are transformed from the FLAPW basis into the maximally localized Wannier function basis. The resulting electronic band structure and texture of the orbital-angular-momentum operator  $\mathbf{L}$  are displayed in Supplementary Fig. 9.

From this realistic tight-binding model, the orbital-momentum-weighted velocity averaged over the Fermi surface (FS) is calculated by

$$\langle v_\alpha L_\beta \rangle_{\text{FS}} = \frac{\sum_{\mathbf{n}\mathbf{k}} f'_{\mathbf{n}\mathbf{k}} \langle \mathbf{n}\mathbf{k} | (v_\alpha L_\beta + L_\beta v_\alpha) / 2 | \mathbf{n}\mathbf{k} \rangle}{\sum_{\mathbf{n}\mathbf{k}} f'_{\mathbf{n}\mathbf{k}}}, \quad (13)$$

where  $v_\alpha$  and  $L_\beta$  are the  $\alpha$  component of the velocity and the  $\beta$  component of the orbital-angular-momentum operators, respectively. The  $|\mathbf{n}\mathbf{k}\rangle$  is the eigenstate of the Hamiltonian with energy  $E_{\mathbf{n}\mathbf{k}}$  and band

index  $n$ , and  $f'_{\mathbf{n}\mathbf{k}}$  is the energy derivative of the Fermi–Dirac distribution function. To polarize  $L_\beta$ , we add a small orbital Zeeman coupling along the  $\beta$  direction to the bare Hamiltonian. We confirm that the result of equation (13) changes by less than 1% when the orbital Zeeman splitting is increased from 10 meV to 30 meV. The  $\mathbf{k}$ -space integrals in equation (13) are performed on a  $256 \times 256 \times 256$  mesh.

The orbital velocity is estimated by

$$\langle v_\alpha^{L_\beta} \rangle_{\text{FS}} = \frac{\langle v_\alpha L_\beta \rangle_{\text{FS}}}{\sqrt{\langle L_\beta^2 \rangle_{\text{FS}}}}, \quad (14)$$

where  $\langle L_\beta^2 \rangle_{\text{FS}}$  is obtained by equation (13), but with  $v_\alpha$  replaced by  $L_\beta$ . The result is shown in Supplementary Fig. 10.

### Details of ab initio LCC calculations

A thin W stack of 19 body-centred cubic (110) atomic layers is calculated by the self-consistent ab initio method using the same FLAPW parameters as for the bulk calculation given previously, except for the mesh of  $\mathbf{k}$ -points for which we use a  $24 \times 24$  Monkhorst–Pack mesh. For Wannierization, we obtain 342 maximally localized Wannier functions, starting from Wannier states with  $s, p_x, p_y, p_z, d_{z^2}, d_{x^2-y^2}, d_{xy}, d_{yz}, d_{zx}$  symmetries for spin up and down as the initial guess. We define the maximum of the inner window at 2 eV above the Fermi energy.

From the Hamiltonian of the W thin film, the  $\mathbf{k}$ -space orbital-angular-momentum texture at the Fermi surface is obtained by

$$\langle \mathbf{L}_{\text{top}} \rangle_{\text{FS}}(\mathbf{k}) = -4k_B T \sum_n f'_{\mathbf{n}\mathbf{k}} \langle \mathbf{L}_{\text{top}} \rangle_{\mathbf{n}\mathbf{k}}, \quad (15)$$

where  $\langle \mathbf{L}_{\text{top}} \rangle_{\mathbf{n}\mathbf{k}} = \langle \mathbf{n}\mathbf{k} | \mathbf{L}_{\text{top}} | \mathbf{n}\mathbf{k} \rangle$  is the expectation value of the orbital angular momentum for the two atoms on the top surface,  $T = 300$  K is temperature, and  $k_B$  is the Boltzmann constant.

To calculate the charge current due to LCC, we consider the orbital-dependent chemical potential

$$\frac{\varepsilon_{\beta\gamma}}{2} (r_\beta L_\gamma + L_\gamma r_\beta) \quad (16)$$

as a perturbation. Here,  $L_\gamma$  is the  $\gamma$  component of the orbital-angular-momentum operator, and  $r_\beta$  is the  $\beta$  component of the position operator, which is well-defined along the  $z$  axis (Fig. 1), and  $\varepsilon_{\beta\gamma}$  can be interpreted as an orbital-dependent electric field. The charge-current density along the  $\alpha$  direction is given by the Kubo formula

$$\langle j_\alpha \rangle = -\frac{e}{V} \sum_{\mathbf{k}\mathbf{n}\mathbf{n}'} (f_{\mathbf{n}\mathbf{k}} - f_{\mathbf{n}'\mathbf{k}}) \text{Re} \frac{\langle \mathbf{n}\mathbf{k} | v_\alpha | \mathbf{n}'\mathbf{k} \rangle \langle \mathbf{n}'\mathbf{k} | V | \mathbf{n}\mathbf{k} \rangle}{E_{\mathbf{n}\mathbf{k}} - E_{\mathbf{n}'\mathbf{k}} + i\Gamma} \quad (17)$$

where  $V$  is the volume of the system and  $\Gamma = 25$  meV is a phenomenological broadening parameter. The LCC response is characterized by the tensor

$$\sigma_{LCC, \alpha\beta}^{L_\gamma} = -\frac{e}{2V} \sum_{\mathbf{k}\mathbf{n}\mathbf{n}'} (f_{\mathbf{n}\mathbf{k}} - f_{\mathbf{n}'\mathbf{k}}) \text{Re} \frac{\langle \mathbf{n}\mathbf{k}, |, v_\alpha, |, \mathbf{n}'\mathbf{k} \rangle \langle \mathbf{n}'\mathbf{k}, |, (r_\beta L_\gamma + L_\gamma r_\beta), |, \mathbf{n}\mathbf{k} \rangle}{E_{\mathbf{n}\mathbf{k}} - E_{\mathbf{n}'\mathbf{k}} + i\Gamma}, \quad (18)$$

which relates  $\langle j_\alpha \rangle$  and  $\varepsilon_{\beta\gamma}$  by  $\langle j_\alpha \rangle = \sigma_{LCC, \alpha\beta}^{L_\gamma} \varepsilon_{\beta\gamma}$ . The  $\mathbf{k}$ -space integral is performed on a  $400 \times 400$  mesh. The  $z$ -resolved LCC response is shown in Supplementary Fig. 11.

### Reporting summary

Further information on research design is available in the Nature Portfolio Reporting Summary linked to this article.

## Data availability

The data that support the plots in the main text of this paper are openly available in Zenodo at <https://doi.org/10.5281/zenodo.8020863>. The data that support other findings of this study are available from the corresponding author on request.

## Code availability

Custom computer codes or algorithms used to generate results that are reported in the paper and central to its main claims are available from the corresponding author on request.

## References

- Naftaly, M. & Miles, R. E. Terahertz time-domain spectroscopy of silicate glasses and the relationship to material properties. *J. Appl. Phys.* **102**, 043517 (2007).
- Lin, Z., Zhigilei, L. V. & Celli, V. Electron-phonon coupling and electron heat capacity of metals under conditions of strong electron-phonon nonequilibrium. *Phys. Rev. B* **77**, 075133 (2008).
- Ordal, M. A. et al. Optical properties of the metals Al, Co, Cu, Au, Fe, Pb, Ni, Pd, Pt, Ag, Ti, and W in the infrared and far infrared. *Appl. Opt.* **22**, 1099–1119 (1983).
- Wimmer, E., Krakauer, H., Weinert, M. & Freeman, A. Full-potential self-consistent linearized-augmented-plane-wave method for calculating the electronic structure of molecules and surfaces: O<sub>2</sub> molecule. *Phys. Rev. B* **24**, 864–875 (1981).
- Perdew, J. P., Burke, K. & Ernzerhof, M. Generalized gradient approximation made simple. *Phys. Rev. Lett.* **77**, 3865–3868 (1996).
- Pizzi, G. et al. Wannier90 as a community code: new features and applications. *J. Phys. Condens. Matter* **32**, 165902 (2020).

## Acknowledgements

We thank G. Sala and P. Brouwer for fruitful discussions. T.S.S., R.R. and T.K. acknowledge funding by the German Research Foundation (DFG) through the collaborative research centre SFB TRR 227 ‘Ultrafast spin dynamics’ (project no. 328545488, projects A05 and B02) and financial support from the Horizon 2020 Framework

Program of the European Commission under the Future and Emerging Technologies programme, open grant no. 863155 (s-Nebula). D.G., F.F. and Y.M. acknowledge the DFG collaborative research centre SFB TRR 173/2 ‘Spin+X’ (project no. 268565370, project A11). K.A. and H.H. acknowledge funding by the Japan Society for the Promotion of Science (grant nos. 22H04964 and 20J20663) and Spintronics Research Network of Japan.

## Author contributions

T.S.S., D.G. and T.K. conceived the idea. T.S.S. designed and conducted the experiments. K.A., T.K. and D.G. gave advice on the experiments. H.H. and K.A. grew the samples. D.G., Y.M. and F.F. performed the ab initio calculations. T.K. derived the analytical model, and T.S.S. and R.R. performed simulations with it. T.S.S. and T.K. cowrote the manuscript, and all authors contributed to the discussion and revision of the manuscript.

## Funding

Open access funding provided by Freie Universität Berlin.

## Competing interests

The authors declare no competing interests.

## Additional information

**Supplementary information** The online version contains supplementary material available at <https://doi.org/10.1038/s41565-023-01470-8>.

**Correspondence and requests for materials** should be addressed to Tom S. Seifert.

**Peer review information** *Nature Nanotechnology* thanks the anonymous reviewers for their contribution to the peer review of this work.

**Reprints and permissions information** is available at [www.nature.com/reprints](http://www.nature.com/reprints).

## Lasing Reporting Summary

Nature Research wishes to improve the reproducibility of the work that we publish. This form is intended for publication with all accepted papers reporting claims of lasing and provides structure for consistency and transparency in reporting. Some list items might not apply to an individual manuscript, but all fields must be completed for clarity.

For further information on Nature Research policies, including our [data availability policy](#), see [Authors & Referees](#).

### ► Experimental design

#### Please check: are the following details reported in the manuscript?

##### 1. Threshold

Plots of device output power versus pump power over a wide range of values indicating a clear threshold

Yes not subject of this study  
 No

##### 2. Linewidth narrowing

Plots of spectral power density for the emission at pump powers below, around, and above the lasing threshold, indicating a clear linewidth narrowing at threshold

Yes not subject of this study  
 No

Resolution of the spectrometer used to make spectral measurements

Yes not subject of this study  
 No

##### 3. Coherent emission

Measurements of the coherence and/or polarization of the emission

Yes Figure S3  
 No

##### 4. Beam spatial profile

Image and/or measurement of the spatial shape and profile of the emission, showing a well-defined beam above threshold

Yes not subject of this study  
 No

##### 5. Operating conditions

Description of the laser and pumping conditions  
*Continuous-wave, pulsed, temperature of operation*

Yes Section "Experimental details" in the main text  
 No

Threshold values provided as density values (e.g.  $W\text{ cm}^{-2}$  or  $J\text{ cm}^{-2}$ ) taking into account the area of the device

Yes not subject of this study  
 No

##### 6. Alternative explanations

Reasoning as to why alternative explanations have been ruled out as responsible for the emission characteristics  
*e.g. amplified spontaneous, directional scattering; modification of fluorescence spectrum by the cavity*

Yes not subject of this study  
 No

##### 7. Theoretical analysis

Theoretical analysis that ensures that the experimental values measured are realistic and reasonable  
*e.g. laser threshold, linewidth, cavity gain-loss, efficiency*

Yes not subject of this study  
 No

##### 8. Statistics

Number of devices fabricated and tested

Yes not subject of this study  
 No

Statistical analysis of the device performance and lifetime (time to failure)

Yes not subject of this study  
 No

